Effect of vapor bubbles on velocity fluctuations and dissipation rates in bubbly Rayleigh-Bénard convection

Rajaram Lakkaraju,[1,*] Laura E. Schmidt,[1] Paolo Oresta,[2,3] Federico Toschi,[4]
Roberto Verzicco,[1,5] Detlef Lohse,[1] and Andrea Prosperetti[1,6,†]

[1]*Physics of Fluids Group, Faculty of Science and Technology, Impact and Mesa+ Institutes, and J. M. Burgers Center for Fluid Dynamics, University of Twente, NL-7500 AE Enschede, The Netherlands*

[2]*Dipartimento di Ingegneria dell' Ambiente e per lo Sviluppo Sostenibile, Politecnico di Bari, Via De Gasperi, I-74123 Taranto, Italy*

[3]*Dipartimento di Ingegneria dell'Innovazione, Universitá del Salento, Via per Arnesano, I-73100 Lecce, Italy*

[4]*Department of Physics, Department of Mathematics and Computer Science, and J. M. Burgers Center for Fluid Dynamics, Eindhoven University of Technology, NL-5600 MB Eindhoven, The Netherlands*

[5]*Department of Mechanical Engineering, University of Rome "Tor Vergata", Via del Politecnico 1, I-00133 Rome, Italy*

[6]*Department of Mechanical Engineering, Johns Hopkins University, Baltimore, Maryland 21218, USA*

(Received 27 June 2011; published 19 September 2011)

Numerical results for kinetic and thermal energy dissipation rates in bubbly Rayleigh-Bénard convection are reported. Bubbles have a twofold effect on the flow: on the one hand, they absorb or release heat to the surrounding liquid phase, thus tending to decrease the temperature differences responsible for the convective motion; but on the other hand, the absorbed heat causes the bubbles to grow, thus increasing their buoyancy and enhancing turbulence (or, more properly, pseudoturbulence) by generating velocity fluctuations. This enhancement depends on the ratio of the sensible heat to the latent heat of the phase change, given by the Jakob number, which determines the dynamics of the bubble growth.

DOI: 10.1103/PhysRevE.84.036312 PACS number(s): 47.55.P−, 47.55.dp, 47.55.Kf

I. INTRODUCTION

It is well known that boiling is a very efficient heat transfer process [1,2]. Bubbles growing near the heated surface absorb latent heat and cool it. Furthermore, the buoyant rise of the bubbles induces a turbulent, or pseudoturbulent, motion in the liquid which brings cooler liquid from the bulk closer to the heated wall and mixes it. The physics involved in this process is very rich and complex and still far from being completely understood. In this paper, which is a continuation of our earlier studies [3,4], we focus on the second aspect, namely the fluctuating motion induced by the bubbles and their thermal interaction with the surrounding liquid. For this purpose we consider a standard Rayleigh-Bénard setting in which a liquid undergoes natural convection in a cell, the base of which is warmer than the top. Vapor bubbles are introduced in this flow and their effect on it is studied numerically. Recent experimental results on a similar system also show an enhanced heat transport compared with single-phase natural convection [5].

Several papers exist on the buoyant rise of gas bubbles and their effect on the liquid motion [6–11]. What distinguishes the present work is that the mechanical coupling between the bubbles and the liquid is augmented and influenced by the thermal coupling, which causes the bubble volume to change. In the following, we first discuss briefly the mathematical formulation and numerical method and then focus on how bubbles promote turbulence and liquid velocity and temperature fluctuations in the Rayleigh-Bénard convection inside a cylindrical cell.

II. GOVERNING EQUATIONS AND NUMERICAL METHOD

Details about the model used in this work can be found in [3]. The governing equations for the incompressible fluid flow under the Boussinesq approximation, augmented by the momentum and energy effects of the two-way coupled, pointlike bubbles, are [3,12]

$$\nabla \cdot \mathbf{u} = 0, \tag{1}$$

$$\frac{D\mathbf{u}}{Dt} = -\frac{1}{\rho}\nabla p + \nu\nabla^2\mathbf{u} + \beta(T - T_{\rm sat})\mathbf{g} + \frac{1}{\rho}\sum_{i=1}^{N}\mathbf{f}_i\delta(\mathbf{x} - \mathbf{x}_i), \tag{2}$$

$$\frac{DT}{Dt} = \frac{\kappa}{\rho c_p}\nabla^2 T + \frac{1}{\rho c_p}\sum_{i=1}^{N}\mathbf{Q}_i\delta(\mathbf{x} - \mathbf{x}_i). \tag{3}$$

Here $\mathbf{u}$, p, and T are the liquid velocity, pressure, and temperature fields; ρ, ν, κ, and c_p are the (constant) liquid density, kinematic viscosity, thermal conductivity, and specific heat; β is the isobaric thermal expansion coefficient; and N is the total number of bubbles. The mechanical and thermal forcings at the location $\mathbf{x}_i$ of the ith bubble are given by $\mathbf{f}_i = \frac{4}{3}\pi r_{b_i}^3\rho([D\mathbf{u}/Dt]_{\mathbf{x}_i} - \mathbf{g})$ and $\mathbf{Q}_i = 4\pi r_{b_i}^2 h_{b_i}(T_{\rm sat} - T_i)$, respectively. Here r_{b_i} is the radius of the ith bubble, T_i the liquid temperature at the bubble location, and h_{b_i} the bubble convective heat transfer coefficient; $T_{\rm sat}$ is the saturation temperature at the system's pressure.

The bubbles are tracked by solving the following dynamical equation in which their mass is neglected (see, e.g., [13]):

$$C_A\rho\left[\frac{4}{3}\pi r_{b_i}^3\left(\frac{D\mathbf{u}}{Dt} - \frac{d\mathbf{V}}{dt}\right) + (\mathbf{u} - \mathbf{V})\frac{d}{dt}\left(\frac{4}{3}\pi r_{b_i}^3\right)\right] - \frac{1}{2}\pi C_D\rho r_{b_i}^2|\,\mathbf{V} - \mathbf{u}\,|(\mathbf{V} - \mathbf{u}) + \frac{4}{3}\pi r_{b_i}^3\rho\frac{D\mathbf{u}}{Dt} + C_L\frac{4}{3}\pi r_{b_i}^3\rho(\nabla\times\mathbf{u})\times(\mathbf{V} - \mathbf{u}) - \frac{4}{3}\pi r_{b_i}^3\rho\mathbf{g} = 0 \tag{4}$$

*r.lakkaraju@tnw.utwente.nl
†prosperetti@jhu.edu

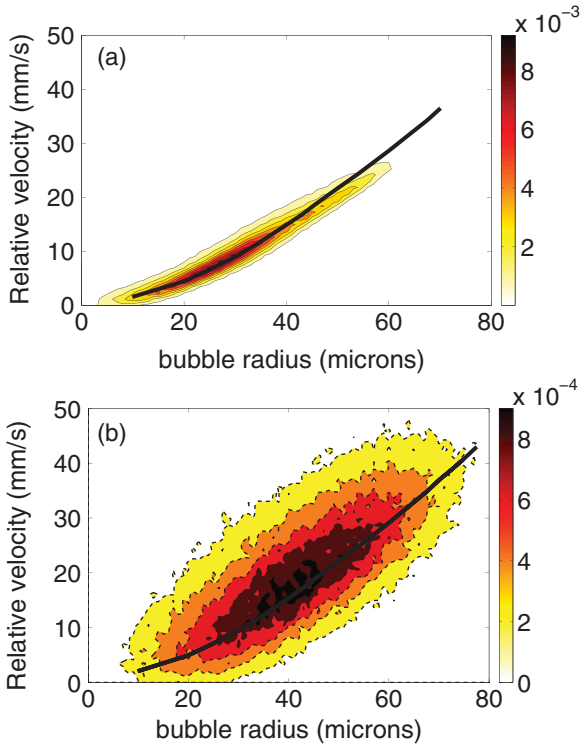

FIG. 1. (Color online) Isolines of the bubble probability density function in the radius-relative velocity plane for Ja = 0.1 (a) and Ja = 1 (b). The solid black line shows the terminal velocity in a quiescent fluid. The bubbles are injected with an initial radius of 12.5 μm.

in which $C_A = 1/2$ and $C_L = 1/2$ are the added mass and lift coefficients, respectively [14,15]. The drag coefficient is modeled as mentioned in [16,17] as follows:

$$C_D = \frac{16}{\mathrm{Re}_b}\left[1 + \frac{\mathrm{Re}_b}{8 + \frac{1}{2}(\mathrm{Re}_b + 3.315\sqrt{\mathrm{Re}_b})}\right] \tag{5}$$

in which $\mathrm{Re}_b = 2r_b \mid \mathbf{V} - \mathbf{u} \mid /\nu$, with $\mathbf{V}$ the bubble velocity, is the bubble Reynolds number.

In view of the small temperature differences, the radial inertia of the bubbles can be neglected, which implies that the vapor pressure inside the bubble equals the local ambient value. This quasiequilibrium relation should be corrected for the effect of surface tension, but we neglect this feature for simplicity and also so as not to obscure, by the introduction of a fairly minor effect, the impact of bubble growth on the dynamics of the system under consideration. For example, for bubbles with a typical size of 50 μm (see, e.g., Fig. 1) the surface tension overpressure amounts to about 2% of 1 atm. The parameter values specified below show that, in the present simulations, flow-induced pressure changes are small and so are hydrostatic effects, so the vapor pressure can be assumed to remain essentially constant. As a consequence, because the vapor is at saturation, the bubble wall temperature can be taken to be the saturation temperature T_{sat} at the ambient pressure. The evolution of the bubble radius can therefore be directly linked to the thermal energy exchange with the liquid by

$$L\frac{d}{dt}\left(\frac{4}{3}\pi r_{b_i}^3 \rho_V\right) = 4\pi r_{b_i}^2 h_{b_i}(T_i - T_{\mathrm{sat}}) \tag{6}$$

in which L is the latent heat of the liquid and ρ_V the vapor density.

The heat transfer coefficient of each bubble is expressed in terms of the Nusselt number,

$$\mathrm{Nu}_b = \frac{2r_b h_b}{\kappa}, \tag{7}$$

by a semiempirical formula which interpolates between the value $\mathrm{Nu}_b = 2$ at very low Jakob numbers and small relative velocities and

$$\mathrm{Nu}_b = 2\sqrt{\frac{2r_b|\mathbf{V} - \mathbf{u}|}{\pi\kappa}} \tag{8}$$

at large relative velocities; see [3] for details.

Our use of the point particle approximation is justified by the facts that the Kolmogorov length scale is always larger than the bubble mean radius and, second, that the volume fraction for the bubble phase is at most only 0.2% (see, e.g., [18]).

The numerical treatment of the equations follows that described in [19,20] and in [3]. Briefly, the field equations are discretized in space by a second-order finite difference scheme based on the projection method on a nonuniform staggered grid with $33 \times 25 \times 65$ points in the azimuthal, radial, and axial directions, respectively. Time is advanced by the third-order Runge-Kutta scheme with a constant nondimensional time step of 2×10^{-4} dimensionless time units. The adequacy of this spatial and temporal discretization was demonstrated in [3] and a further test is described later.

In each computational cell the forces exerted by the bubbles on the liquid are replaced by an equivalent system of forces at the grid nodes constructed in such a way as to produce the same net resultant and couple on the liquid as the original forces (see [3]). An analogous strategy is followed for the bubble-related sources in the right-hand side of the energy equation (3) so that the total amount of heat that each bubble exchanges with the liquid is preserved. The interpolations used in these steps are second-order accurate and therefore consistent with the overall spatial accuracy of the discretization.

Bubbles are removed when they reach the top plate of the cell and reinjected with their lower surface tangent to the bottom plate with the local fluid velocity and an initial radius of 12.5 μm (see [3]). The results were found to be insensitive to the bubble injection size, which was varied between 6.5 and 25 μm in a few cases. The initial injection location was chosen randomly from a uniform distribution.

The saturation temperature T_{sat} was taken as 100 °C, namely the saturation temperature of water at normal pressure, while the bottom (hot) and top (cold) boundary temperatures T_H and T_C were taken as $T_H = T_{\mathrm{sat}} + \frac{1}{2}\Delta T$ and $T_C = T_{\mathrm{sat}} - \frac{1}{2}\Delta T$, respectively, with $\Delta T = 0.25$ K. This temperature difference would not correspond to a realistic boiling situation, but it enables us to focus on the physics of the bubble-induced flow at an affordable computational cost. The fluid properties used are those of water at 100 °C.

The simulations were conducted in a cylindrical cell with an aspect (diameter-to-height) ratio of $d/H = 1/2$; the height was 17.9 mm. The equations were solved for fixed Rayleigh number, $\mathrm{Ra} = g\beta(T_H - T_C)H^3/\nu\kappa$, and Prandtl number, $\mathrm{Pr} = \nu/\kappa$. The thermal energy balance of the bubble with the

TABLE I. Summary of length and velocity scales for the present simulations for different Jakob numbers. H is the cell height, η the Kolmogorov length scale, λ the Taylor length scale, $\overline{r}_b$ the bubble radius averaged over time and over all the bubbles, $\langle u' \rangle_{t,V}$ the time- and volume-averaged rms liquid velocity fluctuation, $\overline{V}_r$ the mean bubble-liquid vertical relative velocity, and Re_λ the Taylor Reynolds number.

Ja	$10^2\overline{r}_b/H$	$10^2\eta/H$	$10^2\lambda/H$	$\langle u' \rangle_{t,V}/\overline{V}_r$	Re_λ
0.00	0.071	6.16		0.004	
0.10	0.22	0.77	3.31	0.20	4.79
0.15	0.24	0.68	3.43	0.21	6.49
0.20	0.26	0.64	3.82	0.22	9.28
0.25	0.27	0.60	3.89	0.23	10.76
0.30	0.28	0.58	4.17	0.24	13.42
0.40	0.31	0.54	4.39	0.24	17.15
0.60	0.34	0.49	4.90	0.26	25.97
0.80	0.37	0.46	5.34	0.27	35.57
1.00	0.39	0.45	5.62	0.28	40.03

surrounding fluid, Eq. (6), introduces a third parameter, the Jakob number,

$$\mathrm{Ja} = \frac{\rho c_p (T_H - T_{\mathrm{sat}})}{\rho_V L}, \tag{9}$$

which controls the bubble growth rate. For $\mathrm{Ja} = 0$, the latent heat is infinite and bubbles cannot grow or shrink.

Velocities are nondimensionalized by the so-called free fall velocity $U = \sqrt{g\beta(T_H - T_C)H}$, lengths by the cylinder height H, and times by H/U.

III. RESULTS

With the data specified above, the Jakob number for a water-vapor system would equal 1.3 approximately. However, in the simulations, we vary the Jakob number for fixed $\mathrm{Ra} = 2 \times 10^5$ and $\mathrm{Pr} = 1.75$ (the value for water at 100 °C) to isolate the effect of bubble volume changes on the flow phenomena. The number of bubbles is kept fixed at 10 000. The vapor volume fraction calculated with the initial bubble radius is about 1.85×10^{-5}.

An additional check on the grid independence of the results was carried out for $\mathrm{Ja} = 1.0$ by comparing the total heat transport for the standard grid with $33 \times 25 \times 65$ cells and a finer grid with $33 \times 40 \times 80$ cells. The statistical properties of the flow were within 0.6%, indicating that the resolution provided by the standard grid is sufficient and the flow scales are properly resolved.

The flow properties (Table I) were calculated once the system had reached a statistical stationary state as revealed by monitoring the total heat transport and the liquid velocity fluctuations. Columns 2, 3, and 4 in the table show the time- and volume-averaged bubble mean radius $\overline{r}_b$, Kolmogorov length scale η, and Taylor length scale $\lambda = \langle u' \rangle_{t,V}/\langle |\nabla u'| \rangle_{t,V}$, respectively. Here and elsewhere in this paper angle brackets denote averages over the variable(s) indicated by the subscripts V for volume, t for time, and, later, A for the cross-sectional area; quantities averaged over all the bubbles and over time are indicated by an overline. The mean liquid velocity fluctuation $\langle u' \rangle_{t,V}$ is defined by

$$\langle u' \rangle = \langle \sqrt{\tfrac{1}{3} \mid \mathbf{u}(\mathbf{x},t) - \langle \mathbf{u} \rangle_t(\mathbf{x}) \mid^2} \rangle_{t,V} \tag{10}$$

and the mean liquid velocity gradient by

$$\langle |\nabla u'| \rangle = \langle \sqrt{\tfrac{1}{3} \mid \nabla \mathbf{u}(\mathbf{x},t) - \langle \nabla \mathbf{u} \rangle_t(\mathbf{x}) \mid^2} \rangle_{t,V}. \tag{11}$$

With the present parameter values, the pattern of the single-phase flow in the cell is a roll with an approximately horizontal axis. For reasons explained below, the introduction of bubbles with $\mathrm{Ja} = 0$, which forces them to maintain a fixed radius as noted before, modifies the flow pattern to a toroidal vortex with the descending stream near the axis and the ascending stream in the surrounding volume. As Ja increases and the bubble volume is allowed to change and, in particular, to grow in the warmer liquid regions, a flow pattern qualitatively similar to the single-phase one but with higher velocities is gradually established. As they are introduced at the hot plate, bubbles are swept up by the annular roll, adding to its buoyancy and thereby increasing the intensity of the circulation. It is also found that in this regime the axis of the roll rotates in a horizontal plane, as in single-phase Rayleigh-Bénard flow [21].

For $\mathrm{Ja} = 0$ the bubbles maintain the same radius with which they are injected and the vast majority of them rise relative to the liquid with a velocity very close to the terminal velocity of about 1.7 mm/s. To give an impression of the major effect of a nonzero Jakob number on the dynamics of the bubble-liquid interaction, we show in Fig. 1 isolines of the bubble probability density function in the radius-relative velocity plane for $\mathrm{Ja} = 0.1$ [Fig. 1(a)] and $\mathrm{Ja} = 1$ [Fig. 1(b)]. The solid black line in these figures is the terminal velocity as given by a balance of buoyancy and drag as computed from Eq. (5). As bubble growth and, with it, increased buoyancy are allowed, the spread of the bubbles' velocity relative to that of the liquid increases considerably. This feature demonstrates the increasing importance of the additional forces present in the bubble equation of motion (4) with increasing bubble volume.

A measure of the turbulence intensity is given by the ratio $\langle u' \rangle_{t,V}/\overline{V}_r$, where $\overline{V}_r$ is the mean bubble-liquid vertical relative velocity given by

$$\overline{V}_r = \left\langle \frac{1}{N} \sum_{i=1}^{N} |V_{z,i}(t) - u_{z,i}(t)| \right\rangle_t. \tag{12}$$

Column 5 of Table I shows that, in the present simulations, this quantity is small for $\mathrm{Ja} = 0$ which, as noted above, corresponds to nongrowing bubbles, but becomes of the order of 20–30% as Ja increases to 1. Note that here the turbulence intensity is larger than in the case of pseudoturbulence without heating and with periodic boundary conditions in all directions [9], where $\langle u' \rangle_{t,V}/\overline{V}_r$ was found to be of the order of 6%. In that work [9], which was quantitatively confirmed by independent simulations by Calzavarini [22], the bubbles did not grow and the drag law was pure Stokes. We have repeated our simulations with $\mathrm{Ja} = 0$ and the same drag law, still finding considerably larger velocity fluctuations than reported for the case of pseudoturbulence with periodic boundary conditions and no heating. Thus we conclude that the reason for this

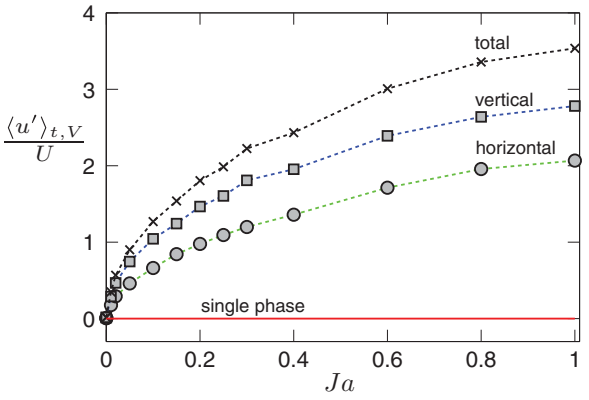

FIG. 2. (Color online) The volume- and time-averaged horizontal (○), vertical (□) and total (×) velocity fluctuations as functions of the Jakob number.

difference lies in the nature of the two flows investigated. The work of [9] concerns the rise of fixed-radius bubbles in a quiescent liquid in a cube with periodic boundary conditions not only on the sides but also on the top and bottom. In that system the only liquid flow is induced by the bubbles and, in a frame of reference with zero mean flow, the bubbles rise while, by continuity, the liquid descends. The velocity of the two phases is therefore mostly parallel and the bubbles distribute statistically uniformly (but of course accumulate in vortices, which however are statistically uniformly distributed over the flow volume). In the present system, on the other hand, liquid flow is driven by buoyancy in addition to the bubbles, and the presence of impervious top and bottom boundaries causes the appearance of regions where the tendency of the bubbles to rise encounters nearly horizontal mean liquid streamlines. As noted before, bubbles are also swept up by the ascending convection current as they are introduced at the bottom boundary. All of these factors cause a much more complex situation and presumably marked nonuniformities in the vortex and thus also bubble distribution. We believe that this is the explanation for the difference between the present work and that of [9]. The velocity fluctuations of course increase substantially when the bubbles are allowed to grow.

It is also interesting to note that the velocity fluctuations are far from isotropic. Figure 2 shows the volume- and time-averaged liquid velocity fluctuations in the vertical and horizontal directions. The fluctuations become more and more anisotropic with increasing Jakob number. Velocity fluctuations for the single-phase case are basically zero as the flow is essentially laminar for the Rayleigh number used here.

The normalized time- and volume-averaged kinetic energy dissipation rate $\langle \epsilon_K \rangle_{t,V} = \nu \langle | \nabla \mathbf{u} |^2 \rangle_{t,V}$ is shown as a function of the Jakob number in Fig. 3. For comparison, the energy dissipation rate for single-phase convection is also shown by the continuous line. It can be observed that dissipation in the bubbly flow is generally higher than for the single-phase flow. However, for very small Jakob numbers, the opposite behavior is found as Fig. 3(b) shows: for these Jakob numbers energy dissipation is less, which implies that turbulence is attenuated. The explanation is that, for $\mathrm{Ja} = 0$, the bubbles have an effectively infinite heat capacity and therefore they can

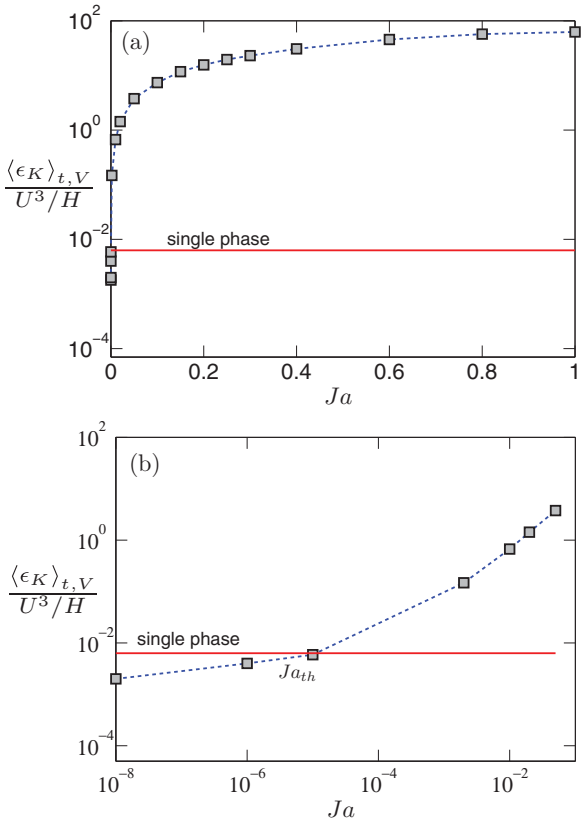

FIG. 3. (Color online) (a) Normalized kinetic energy dissipation rate as a function of the Jakob number Ja. (b) Energy dissipation rate for very low Ja, $10^{-8} \leqslant \mathrm{Ja} \leqslant 10^{-2}$ on a log-log scale. In both graphs the horizontal solid line shows the single-phase value for reference.

absorb or release heat to the surrounding fluid while remaining at T_{sat}, which also equals the mean temperature of the hot and the cold plates. The net effect is a tendency to "short-circuit" the temperature difference and, therefore, a tendency to the quenching of the natural convection. The same effect was found in [3]. This process is responsible for the transition mentioned earlier from the annular roll of the single-phase case to the lower-energy toroidal roll prevailing for small Ja. The tendency of the bubbles to reduce temperature differences is always present but, with increasing Ja, it is overshadowed by the increased buoyancy provided to the two-phase medium. The bubbles rise faster and, by mechanically stirring the liquid phase, increase the kinetic energy dissipation rate.

The normalized time- and volume-averaged thermal energy dissipation rate $\langle \epsilon_T \rangle_{t,V} = \kappa \langle | \nabla T |^2 \rangle_{t,V}$ is shown as a function of the Jakob number in Fig. 4, where the horizontal solid line is the single-phase result. Unlike the kinetic energy dissipation, even nongrowing bubbles with $\mathrm{Ja} = 0$ slightly increase $\langle \epsilon_T \rangle_{t,V}$. The reason lies in the fact that the bubble surface temperature is fixed, which causes a local cooling or heating of the surrounding liquid.

Figure 5 compares the normalized kinetic energy dissipation rate averaged over the azimuthal angle and time, $H \nu \langle | \nabla \mathbf{u} |^2 \rangle_{t,\theta} / U^3$, in single-phase [Fig. 5(a)] and two-phase flow with $\mathrm{Ja} = 0$ [Fig. 5(b)] and $\mathrm{Ja} = 1$ [Fig. 5(c)]; note the different (color) shaded scales in these three figures. The single-phase annular roll is characterized by a relatively

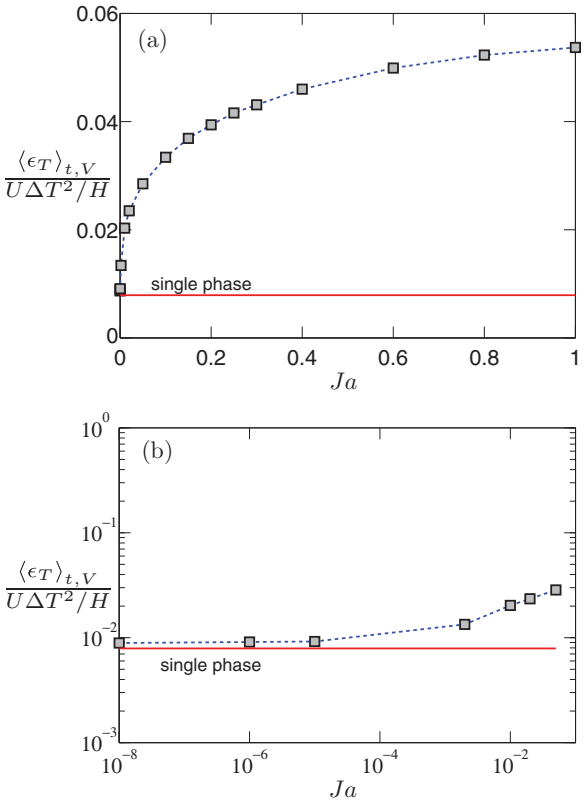

FIG. 4. (Color online) (a) Normalized thermal energy dissipation rate as a function of the Jakob number Ja. (b) Energy dissipation rate for very low Ja, $10^{-8} \leqslant \mathrm{Ja} \leqslant 10^{-2}$ on a log-log scale. In both graphs the horizontal solid line is the single-phase value for reference.

strong dissipation near the boundaries, as expected, and by small dissipation elsewhere. The change to a toroidal roll caused by the introduction of nongrowing bubbles [Fig. 5(b), Ja = 0] results in strong gradients in the relatively thin central region seat of descending flow, surrounded by a larger

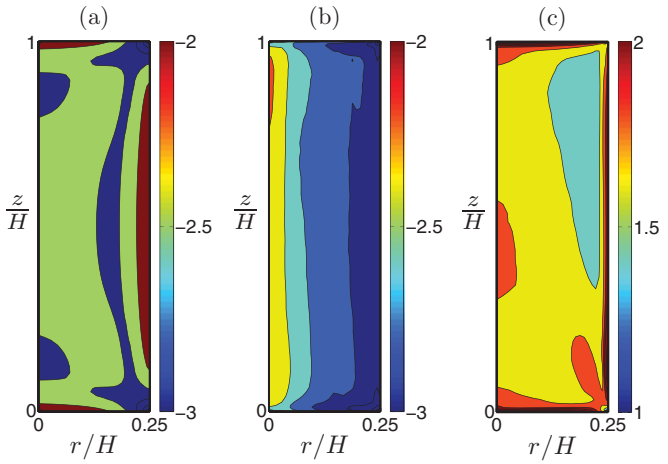

FIG. 5. (Color online) Angle-averaged kinetic energy dissipation $\langle \epsilon_K \rangle_{t,\theta}$ normalized by U^3/H in the r-z plane: (a) single phase, (b) Ja = 0.0 (nongrowing 10^4 bubbles), and (c) Ja = 1.0 (growing 10^4 bubbles). The color scale is logarithmic and it is different in (c) as compared to (a) and (b).

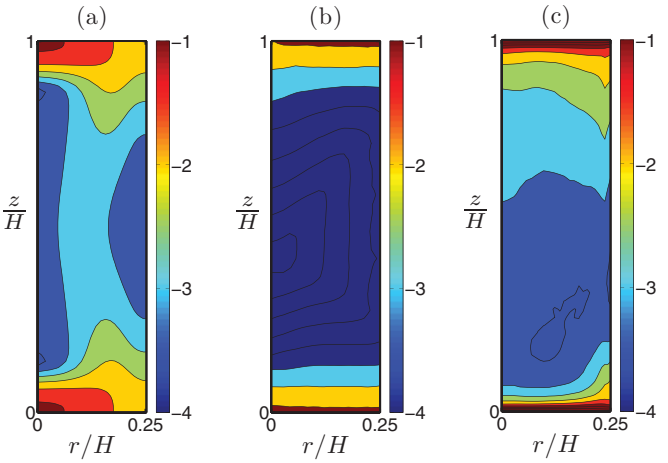

FIG. 6. (Color online) Angle-averaged thermal energy dissipation $\langle \epsilon_T \rangle_{t,\theta}$ normalized by $U\Delta T^2/H$ in the r-z plane: (a) single phase, (b) Ja = 0.0 (nongrowing 10^4 bubbles), and (c) Ja = 1.0 (growing 10^4 bubbles). The (color) shaded scale is logarithmic.

volume of smaller ascending velocities and smaller gradients. Bubbles with Ja = 1 restore a flow pattern with a horizontal roll qualitatively similar to the single-phase one but with higher velocities. The resulting distribution of the dissipation resembles the single-phase one but is considerably higher.

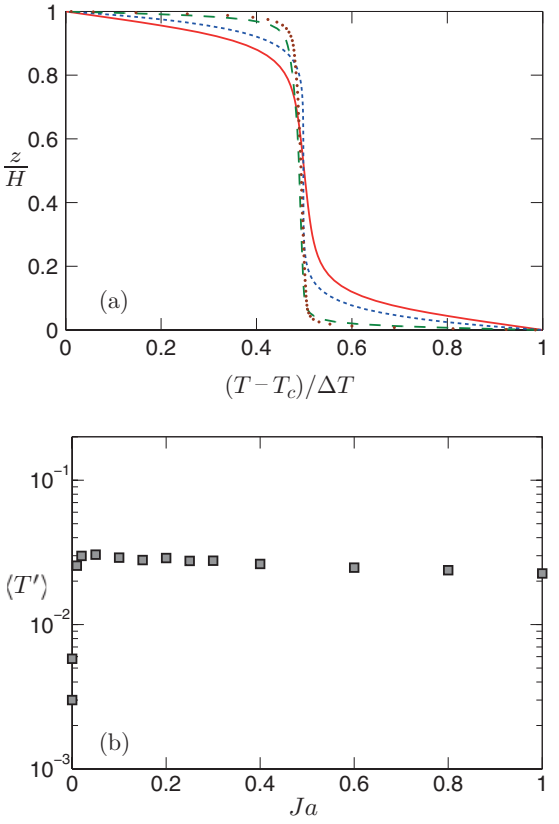

FIG. 7. (Color online) (a) Vertical temperature profile averaged over the horizontal cross section for the single-phase case [solid (red) line], Ja = 0 [short-dashed (blue) line], Ja = 0.1 [long-dashed (green) line], and Ja = 0.8 [dotted (brown) line]. (b) Volume-averaged rms temperature fluctuation, $\langle T' \rangle$, as a function of the Jakob number, on a linear-log scale.

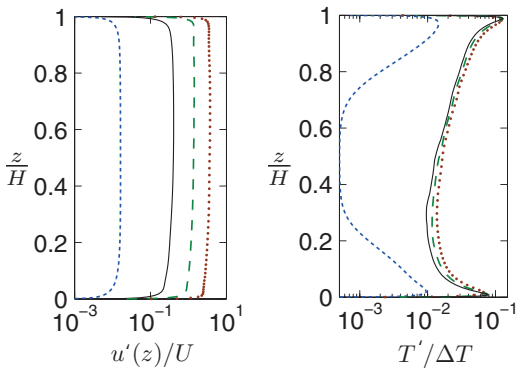

FIG. 8. (Color online) Normalized vertical velocity $u'(z)/U$ and temperature $T'(z)/\Delta T$ fluctuations averaged over the horizontal cross section as functions of the vertical coordinate z: Ja $= 0$ [short-dashed (blue) lines], Ja $= 0.01$ [solid (black) line], Ja $= 0.1$ [long-dashed (green) lines], and Ja $= 0.8$ [dotted (brown) lines].

The normalized thermal energy dissipation rate $H\kappa\langle|\nabla T|^2\rangle_{t,\theta}/(U\Delta T^2)$ averaged over time and the azimuthal direction is shown in Fig. 6. The effects of the large-scale circulation with strong thermal gradients on the hot and cold plates prevailing in the single-phase case can be observed in Fig. 6(a). After introducing nongrowing bubbles (Ja $= 0$), the temperature gradients are smoothed [Fig. 6(b)] and greatly reduced. For growing bubbles [Ja $= 1.0$, Fig. 6(c)] the temperature differences in the bulk region are still smoothed, but the enhanced convection raises the thermal dissipation with respect to the Ja $= 0$ case.

Figure 7(a) shows the vertical temperature profile averaged over the horizontal cross section as a function of z for different Jakob numbers. Figure 7(b) shows the normalized volume- and time-averaged rms temperature fluctuations $\langle T'\rangle = \sqrt{\langle(T-\langle T\rangle_t)^2\rangle_{t,V}}/\Delta T$. The presence of bubbles decreases the thermal boundary layer thickness near both plates even for Ja $= 0$. The origin of this reduction lies in the fact that, since the bubble temperature $T_{\rm sat} = \frac{1}{2}(T_H + T_C)$ remains constant, the mere presence of the bubbles, whether they be allowed to grow or not, has the effect of cooling the liquid near the hot plate and warming it up near the cold one. Of course, the effect increases with Ja and leads to a thinning of the thermal layer.

Figure 8 shows the normalized velocity and temperature fluctuations averaged over time and the horizontal cross section as functions of the vertical coordinate. As expected, the velocity fluctuations [Fig. 8(a)] decrease in the viscous boundary layers near the plate but are otherwise fairly constant and increase with Ja. The temperature fluctuations exhibit marked boundary layers near the plates due to the fact that, with their fixed interface temperature, bubbles behave as "cold spots" or "hot spots" near the bottom or top plates, thus inducing relatively strong temperature differences with respect to the adjacent liquid.

IV. CONCLUSIONS

The present numerical investigation considered the kinetic and thermal energy dissipation rates in a two-phase Rayleigh-Bénard convection in a cylindrical cell, where 10^4 saturated vapor bubbles are injected into the flow. Due to their fixed surface temperature, bubbles tend to smooth the liquid temperature differences by absorbing and releasing heat and add vertical momentum to the flow with their buoyancy. The balance between these competing effects depends on the ratio of the sensible heat to the latent heat of the liquid, as quantified by the Jakob number Ja defined in Eq. (9). For very small Ja, the bubble volume change is small and the absorption or release of heat dominates over the buoyancy effect. The outcome is a reduction of the driving force of the circulation with a corresponding attenuation of the kinetic energy dissipation. The added buoyancy, however, starts becoming dominant already at small Ja with a strong enhancement of the kinetic and thermal energy dissipations.

ACKNOWLEDGMENTS

We thank Leen Van Wijngaarden, Kristjan Gudmundsson, and J. M. Mercado for discussions and acknowledge the National Computing Facilities Foundation (NCF) for allowing us to perform computations on SARA in Amsterdam. This research is part of the Industrial partnership program on Fundamentals of Heterogeneous Bubbly Flows, which is funded by the Foundation for Fundamental Research on Matter (FOM), The Netherlands. Support from FIRB (under Grant No. RBFR08QIP5_001) is gratefully acknowledged.

[1] V. K. Dhir, Annu. Rev. Fluid Mech. **30**, 365 (1998).
[2] J. Kim, Int. J. Multiphase Flow **35**, 1067 (2009).
[3] P. Oresta, R. Verzicco, D. Lohse, and A. Prosperetti, Phys. Rev. E **80**, 026304 (2009).
[4] L. E. Schmidt, P. Oresta, F. Toschi, R. Verzicco, D. Lohse, and A. Prosperetti, New J. Phys. **13**, 025002 (2011).
[5] J. Q. Zhong, D. Funfschilling, and G. Ahlers, Phys. Rev. Lett. **102**, 124501 (2009).
[6] L. Van Wijngaarden, Theor. Comput. Fluid Dyn. **10**, 449 (1998).
[7] E. Climent and J. Magnaudet, Phys. Rev. Lett. **82**, 4827 (1999).
[8] O. Druzhinin and S. E. Elghobashi, J. Fluid Mech. **429**, 23 (2001).
[9] I. M. Mazzitelli and D. Lohse, Phys. Rev. E **79**, 066317 (2009).
[10] F. Toschi and E. Bodenschatz, Annu. Rev. Fluid Mech. **41**, 375 (2009).
[11] J. Martinez-Mercado, D. Chehata Gomez, D. P. M. v. Gils, C. Sun, and D. Lohse, J. Fluid Mech. **650**, 287 (2010).
[12] L. Wang and M. R. Maxey, Appl. Sci. Res. **51**, 291 (1993).
[13] J. Magnaudet and I. Eames, Annu. Rev. Fluid Mech. **32**, 659 (2000).
[14] T. R. Auton, J. Fluid Mech. **183**, 199 (1987).
[15] E. A. Van Nierop, S. Luther, J. J. Blumink, J. Magnaudet, A. Prosperetti, and D. Lohse, J. Fluid Mech. **571**, 439 (2007).

[16] R. Mei, J. F. Klausner, and C. J. Lawrence, Phys. Fluids **6**, 418 (1994).
[17] R. Mei and J. F. Klausner, Phys. Fluids A **4**, 63 (1992).
[18] F. Lucci, A. Ferrante, and S. Elghobashi, J. Fluid Mech. **650**, 5 (2010).
[19] R. Verzicco and P. Orlandi, J. Comput. Phys. **123**, 402 (1996).
[20] R. Verzicco and R. Camussi, J. Fluid Mech. **477**, 19 (2003).
[21] G. Ahlers, S. Grossmann, and D. Lohse, Rev. Mod. Phys. **81**, 503 (2009).
[22] E. Calzavarini (private communication).